Chinese Chemical Letters 35 (2024) 108846

Contents lists available at ScienceDirect

Chinese Chemical Letters

journal homepage: www.elsevier.com/locate/cclet

Self assembled electron blocking and lithiophilic interface towards dendrite-free solid-state lithium battery

Caixia Li[a], Yi Qiu[a], Yufeng Zhao[a,*], Wuliang Feng[a,b,*]

[a] Institute for Sustainable Energy & College of Sciences, Shanghai University, Shanghai 200444, China
[b] Key Laboratory of Advanced Energy Materials Chemistry (Ministry of Education), Nankai University, Tianjin 300071, China

ARTICLE INFO

Article history:
Received 5 June 2023
Revised 11 July 2023
Accepted 24 July 2023
Available online 28 July 2023

Keywords:
$Li_7La_3Zr_2O_{12}$
LiI interphase
Interfacial contact
Li dendrite
Thermodynamic stable

ABSTRACT

The poor interfacial contact is one of the biggest challenges that solid-state lithium batteries suffer from. Reducing the solid-state electrolyte surface energy by transforming the interface from lithiophobic to lithiophilic is effective to promote the interfacial contact, but electronic conductive interphases usually increase the risk of electron attack, thus leading to uncontrollable Li dendrite growth. Herein, we propose a self-assembled thermodynamic stable LiI interphase to simultaneously improve the interfacial contact between the garnet electrolyte $Li_7La_3Zr_2O_{12}$ (LLZO) and Li anode, and prohibit the electron attack. The direct contact between LLZO and Li and the high temperature Li melting process was ascribed to Zr^{4+} reduction, which facilitated Li dendrite formation and propagation. With the modification of the high lithiophilic I_2 thin film, the area specific interfacial resistance of LLZO/Li was reduced from 1525 Ω/cm^2 to 57 Ω/cm^2. More importantly, LLZO was protected from being reduced due to the outstanding electronic insulativity of the LiI interphase, which leaded to a high critical current density of 1.2/7.0 mA/cm^2 in the time/capacity-constant modes, respectively.

To realize the next generation secondary battery with an energy density that exceeds 500 Wh/kg, lithium metal is regarded as the ultimate anode due to its high specific capacity (3860 mAh/g) and low redox potential (−3.04 V *versus* the standard hydrogen electrode) [1–5]. However, huge volume change of Li and side reactions with the conventional liquid electrolyte leads to continuously increased polarization and the formation of isolated Li, which accelerates battery degradation [6–10]. Moreover, the flammability of the organic solvent also brings safety issues [11]. Comparatively, transforming the battery from liquid to solid is promising to exclude the as mentioned worries due to the outstanding Li compatibility and high thermostability of the solid-state electrolytes (SSEs) [12–17].

Possessing the lowest reduction potential against metal Li and high ionic conductivity (10^{-4}–10^{-3} mS/cm), the garnet type SSEs $Li_7La_3Zr_2O_{12}$ (LLZO) has attracted extensive attention in the latest decade [18,19]. However, the high elastic modulus of LLZO lead to the rigid interfacial contact, which hinders the development of the LLZO based solid-state lithium batteries (SSLBs) [20]. Due to the high lithium content in the cubic lattice, LLZO is vulnerable for Li^+/H^+ exchange in ambient air. The as formed LiOH and Li_2CO_3 contaminants are known to be lithiophobic, which lead to huge surface energy and poor Li wettability [21,22]. Even though pristine LLZO is demonstrated to be intrinsically lithiophilic [23], the strategies of surface contaminants eliminations such as mechanical polishing [24], chemical etching [25,26] and carbothermal reactions [27] bring in extra surface defects or reduction phases, which increase the risk of electron attack.

LLZO is once considered to be electrochemical and chemical stable against Li. However, Zr^{4+} and dopants such as Al^{3+} and Nb^{5+} were witnessed to be reduced by Li [28,29]. Introducing with artificial interlayers is the most adopted strategies to promote the interfacial contacts [30–34]. Regardless of improving the interfacial contact, prohibiting the electron attack is more important for the stabilization of the LLZO/Li interface. The kinetic and thermodynamic stabilities of the LLZO/Li interface play a key part in the electrochemical performance of the LLZO based SSLBs. A thermodynamic unstable but kinetic stable interface is beneficial to protect SSEs from being reduced, but the initial side reactions will lead to huge interphase layer and increased polarization [35,36]. A kinetic and thermodynamic unstable interface will lead to continuous side reaction, which is detrimental for battery performance [37–40]. In principle, an interface with both high kinetic and thermodynamic stabilities is desired. Nevertheless, high thermodynamic stability

* Corresponding authors.
E-mail addresses: yufengzhao@shu.edu.cn (Y. Zhao), wuliangfeng@shu.edu.cn (W. Feng).

https://doi.org/10.1016/j.cclet.2023.108846
1001-8417/

will result in high surface energy, which is contradictory with the promotion of interfacial contact [41,42]. In general, the electronic conductors that based on alloys [43] or lithium-carbon composites [44] are mostly adopted in dealing with the LLZO/Li interface issues. The volume expansion of the electronic conductors is beneficial for interfacial contacts but will lead to kinetical instability. Up to now, there still lack of investigation on reconciling the relationships between lithiophilicity and thermodynamic stability. On the contrary, as long as electron attack is not taken into consideration, barely improving the interfacial LLZO/Li contacts is still far from suppressing Li dendrite formation and propagation. In general, electronic conductive modification layer or interphase is beneficial for interfacial contact, but the high thermodynamic instability usually suffers from severe Li dendrite growth because Li nucleates preferentially on the electronic conductor. On the contrary, an electron blocking interphase is either lithiophobic or sluggish in ionic conduction. Consequently, the in-situ formation of the electron blocking but ionic conducting interphase is beneficial for intimate interfacial contact to reduce the interfacial resistance, and high thermodynamic stability to suppress Li dendrite growth.

Herein, a thermodynamic stable but intimately contacted LLZO/Li interface was realized by a self-assembled LiI interphase. Lithiophilic I_2 modification layer was deposited on the LLZO pellet by evaporation and reacted with metal Li to reduce the area specific resistance (ASR) (Fig. S1 in Supporting information). The direct contact between Li and LLZO, as well as the high temperature Li melting process was demonstrated to be responsible for LLZO reduction, which facilitated Li dendrite formation. Comparatively, with the protection of the thermodynamic stable and electron blocking LiI interphase, electron attack in LLZO was effectively inhibited and the critical current density (CCD) was significantly improved. LiI interphase simultaneously realized intimate LLZO/Li contact as well as high thermo-dynamic stability reconciled the contradictory between high surface energy and small interfacial resistance, which resulted in a dendrite-free solid-state battery.

As shown in Fig. 1a, pristine Garnet SSE displayed a poor contact with Li metal due to the poor lithium wettability, which resulted in a large amount of voids and huge interfacial resistance. The insufficient interfacial contact would result in unevenly distributed electric field, thus leading to inhomogeneous Li plating/striping and Li dendrite growth. By contrast, as illustrated in Fig. 1b, with the modification of I_2 layer, the interface showed superior Li wettability as Li metal reacted with I_2 to form an ionic conductive LiI interphase. The presence of LiI interphase contributed to the intimate interfacial contact, which significantly reduced the interfacial resistance and homogenized electric field

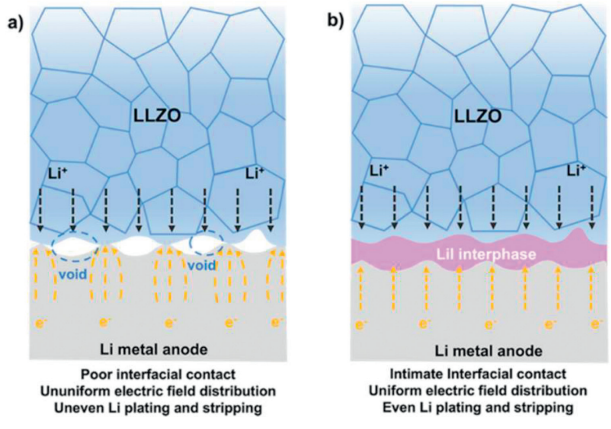

Fig. 1. Schematic illustrations of the (a) pristine LLZO/Li, and (b) I_2 modified LLZO/Li interfaces.

distribution. But more importantly, LiI was demonstrated to be thermo-dynamical stable with metal Li [45]. Therefore, the interfacial reaction would transform the interphase from lithiophilic to lithophobic, and from thermodynamical unstable to stable with high surface energy, which was effective for Li dendrite suppression. In addition, the volume change ratio was calculated to be 126% as the solid expand from I_2 modification layer to the LiI interphase. The volume expansion of the interphase is beneficial for the interfacial contact because as the elimination of interfacial voids.

The X-ray diffraction (XRD) was employed to characterize the phase structure of LLZO. Fig. 2a showed that the XRD pattern of the as sintered LLZO pellet matched with cubic-phase $Li_5La_3Nb_2O_{12}$ (PDF#45-0109), indicating that LLZO was in pure cubic phase and no lithium devoid phase such as $La_2Zr_2O_7$ was formed. Fig. S2 (Supporting information) demonstrated that the as formed interphase was LiI as evidenced by the three new peaks at 29.756°, 42.611° and 50.373°, which were in correspondence with the crystal planes (200), (220) and (311), respectively. Electrochemical impedance spectroscopy (EIS) measurement was applied to study the ionic conductivity of LLZO and the interfacial resistance of the LLZO/Li interface. The ionic conductivity of the as sintered LLZO was calculated to be 3.5×10^{-4} S/cm according to the Nyquist plot in Fig. 2b. The area of LLZO garnet electrolyte was 0.0785 cm^2 and the thickness of was 0.8 mm. The first intersection point of the curve with the real axis represented the bulk resistance of LLZO, and the area specific bulk resistance of sintered LLZO garnet electrolyte was calculated to be 104 Ω/cm^2. The second intersection of the curve with the real axis was the sum of bulk and grain boundary resistance. The area specific resistance of the grain boundary was calculated to be 188 Ω/cm^2. The activation energy of LLZO was measured by linear fitted the ionic conductivity of LLZO with different temperatures according to the Arrhenius equation. As displayed in Fig. 2c, the activation energy of LLZO was calculated to be 0.40 eV. The impedance of the LLZO/Li interface was tested under the Li symmetric cells with and without the I_2 modifications on both sides. The pristine LLZO possessed a huge ASR of 1525 Ω/cm^2 (Fig. 2d). Remarkably, as shown in Fig. 2e, with the modification of I_2, the ASR of the interface was significantly reduced to 57 Ω/cm^2. Such a remarkable decrease in LLZO area specific interface resistance was attributed to the filling of the as formed LiI in the voids between LLZO and Li anode. To optimize the thickness of I_2 modification layer, we characterized the ASR of the LLZO/Li interface with different I_2 modification thicknesses (Fig. 2f). With the increase of I_2 modification layer thickness, the ASR of the LLZO/Li interface displayed a noticeable decrease when the thickness of I_2 was under 0.5 μm while a gradual augment when I_2 thickness was above 0.5 μm. Notably, the ASR of the LLZO/Li interface with I_2 modification layer of 0.25 μm was higher than 0.5 μm. Such a phenomenon could be attributed to the inconsecutive I_2 modification on LLZO, which leaded to a certain area of direct contact between Li with pristine LLZO. When I_2 thickness increased to 0.5 μm, the reduced ASR indicated that the I_2 layer was consecutive and there left no bare pristine LLZO. However, with the increase of I_2 modification thickness, ASR increased gradually on account of the low conductivity of LiI. The conductivity was measured to be 6.8×10^{-8} S/cm according to the Nyquist plot in Fig. S3 (Supporting information). Consequently, 0.5 μm was the optimized I_2 thickness accounting to the advantage of combining superior wettability with adequate conductivity.

The scanning electron microscopy (SEM) in Fig. 3a indicated that the surface of pristine LLZO was smooth. After the deposition of I_2 with a thickness of 0.5 μm, the surface morphology changed greatly with a dense I_2 layer (Fig. 3b). Due to the poor lithium wettability of LLZO, evident voids were observed between LLZO and Li anode (Fig. 3c). With the modification of lithophilic I_2, lithium wettability was improved remarkably. Li anode contacted with the

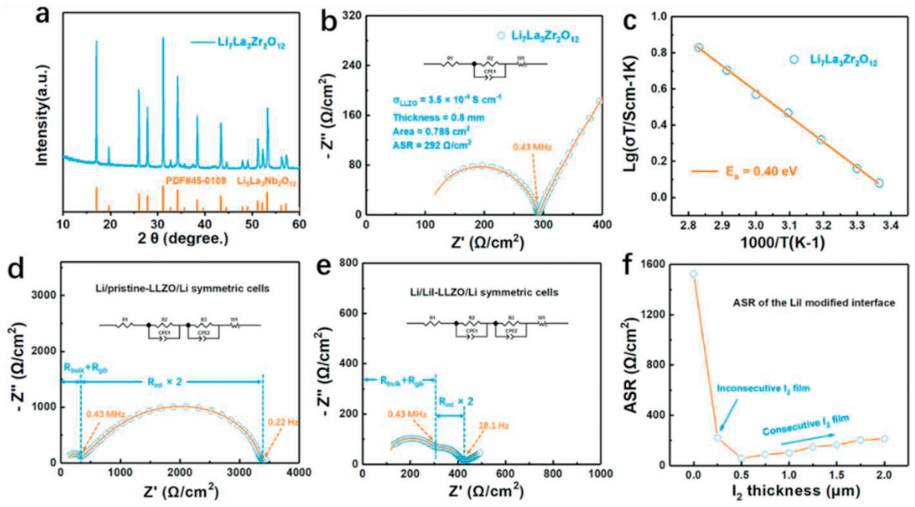

Fig. 2. Characterization of the synthesized LLZO. (a) X-ray diffraction (XRD) pattern, (b) Nyquist plot, and (c) Arrhenius plot of the LLZO pellet. Nyquist plots of (d) Li/Pristine-LLZO/Li and (e) Li/LiI-LLZO/Li symmetric cells. (f) Plot of area specific resistance of the LLZO/Li interface *versus* I_2 modification thickness.

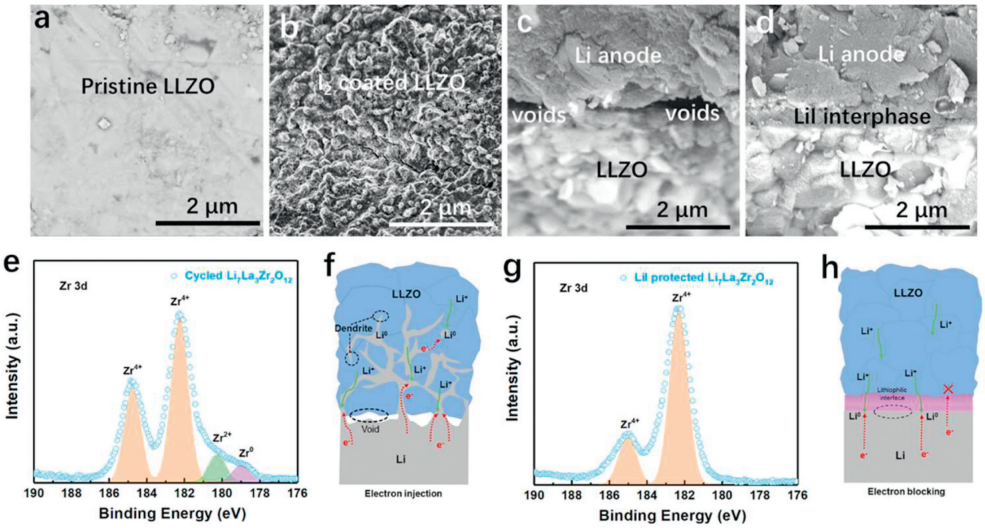

Fig. 3. SEM images of the (a) pristine LLZO, (b) LLZO with I_2 modification layer. Cross-sectional SEM image of (c) pristine-LLZO/Li and (d) LiI-LLZO/Li. X-ray photoelectron spectroscopy (XPS) spectra of Zr 3d for the melting Li contacted LLZO (e) without and (g) with LiI interphase. Schematic illustration of the LLZO&Li contact and Li dendrite growth (f) without, and (h) with LiI interphase.

LLZO garnet electrolyte intimately with the presence of LiI interphase. Fig. 3d displayed that all the voids were filled by LiI. In general, the garnet electrolyte was regarded as thermodynamic stable with metal Li in room temperature. However, there still lack of investigations on thermodynamic stability of garnet/Li interfaces at which the temperature was over Li melting point. Here, XPS was conducted to investigate the valence state of Zr at the LLZO/Li and LiI-LLZO/Li interfaces after cycling. The Zr 3d spectra of cycled LLZO were deconvoluted into four peaks located at 184.5, 182.3, 180.2 and 179.0 eV (Fig. 3e). The peaks located at 184.5 and 182.3 eV were designated to be Zr^{4+}. The peaks at 180.2 and 179.0 eV were indexed to be Zr^{2+} and Zr^{0}, indicating that the pristine LLZO suffered from being reduced when contacting with Li at a high temperature. The reduction phase was detrimental for interfacial stability and could be ascribed to the formation of Li dendrite. As illustrated in Fig. 3f. The voids between LLZO and Li anode leaded to uneven Li plating and stripping. What was worse, electron prone to inject through such reduction phase or grain boundaries to cause Li nucleation inside LLZO, which aggravated Li dendrites penetrate through the LLZO garnet electrolyte. Comparatively, the XPS spectra in Fig. 3g showed only two Zr^{4+} peaks located at 184.5 and 182.3 eV. Chronoamperometry was employed to investigate the electronic conductivity of the pristine LLZO, the reduced LLZO, as well as the LiI interphase. Under a bias voltage of 1 V, the reduced LLZO showed a steady-state current of 2.1×10^{-4} mA, which was more than two magnitudes higher than the pristine LLZO (Fig. S4 in Supporting information). It could be concluded that the reduction phases were responsible for the increased the electronic conductivity. By contrast, the LiI interphase displayed a much smaller steady-state current of 3.92×10^{-7} mA, indicating that the LiI interphase successfully protected LLZO from being reduced when contacting with melted Li and prohibited electron injection (Fig. S5 in Supporting information). Therefore, as demonstrated in Fig. 3h, the modification of I_2 constructed an ionic conductive but electronic insulative LiI interphase between Li anode and LLZO garnet electrolyte, thus improving the interfacial contact and blocking the electron injection effectively.

Li/Pristine-LLZO/Li and Li/LiI-LLZO/Li symmetric cells were cycled galvanostatically to evaluate the interfacial stability. As the time-constant mode CCD test shown in Fig. 4a, the CCD test

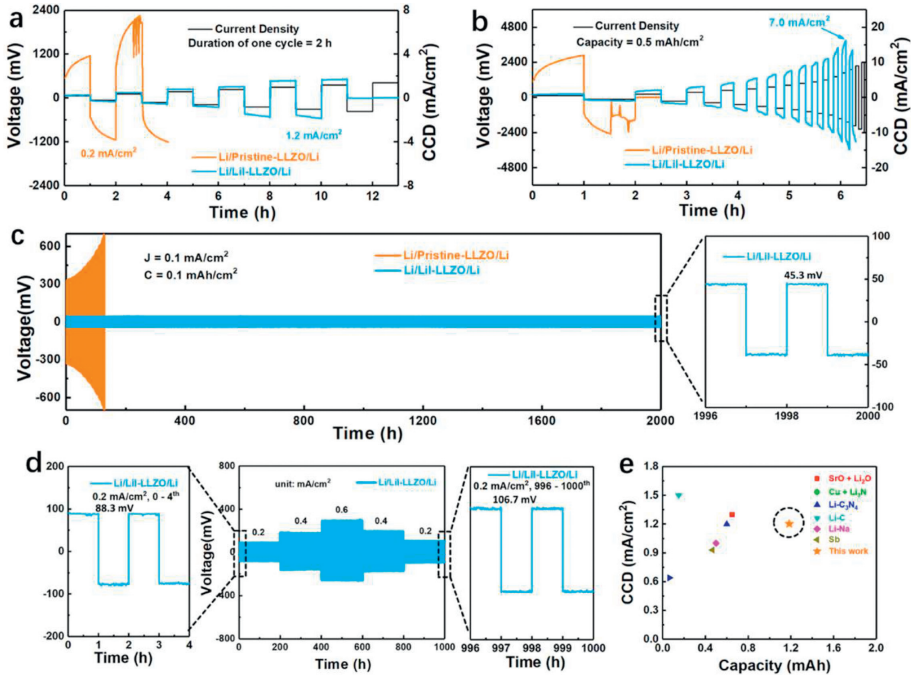

Fig. 4. Electrochemical performance of the Li/Pristine-LLZO/Li and Li/LiI-LLZO/Li symmetric cells. Critical current density (a) in the time-constant mode and (b) in the capacity-constant mode. (c) Galvanostatic cycling stability of the Li/Pristine-LLZO/Li and Li/LiI-LLZO/Li symmetric cells. (d) Voltage profiles of the Li/LiI-LLZO/Li symmetric cell at various current densities and the polarization voltage of the Li/LiI-LLZO/Li symmetric cell operated at the first 4 and the last 4 h. (e) Comparison of the time constant mode CCD value and critical capacity in the related literatures.

stepped every 0.2 mA/cm^2 with a constant charge and discharge period of 1 h. Polarization voltage of Li/Pristine-LLZO/Li sharply increased at 0.2 mA/cm^2, and then short circuited at the second cycling, indicating that the CCD of the Li/Pristine-LLZO/Li symmetric cell was only 0.2 mA/cm^2. Comparatively, Li/LiI-LLZO/Li displayed a smaller overpotential without any sudden changes until stepped to the current density over 1.2 mA/cm^2. As the capacity-constant mode CCD test displayed in Fig. 4b, Li/Pristine-LLZO/Li and Li/LiI-LLZO/Li symmetric cells operated at various current densities with a constant capacity of 0.5 mAh/cm^2. Li/Pristine-LLZO/Li was short circuited at the first cycle. In contrast, the sudden change of overpotential was not observed at Li/LiI-LLZO/Li symmetric cell until the current density was over 7.0 mA/cm^2. In principle, higher relative density will lead to higher ionic conductivity as the reduced grain boundary resistance, and higher critical current density as the reduced internal voids. The critical current density test was performed in room temperature (25 °C). Apart from temperature, the relative density and the thickness of the solid electrolyte, as well as the external pressure also have effect on the value of the critical current density. But considering that all the symmetric cells are assembled and tested in the same condition such as the relative density (95.2%) and the thickness (1 mm) of LLZO, external pressure (1 MPa). The mainly influence factor concentrated on the interfacial contact and the thermodynamic stability. To further investigate the interfacial stability, Li/Pristine-LLZO/Li and Li/LiI-LLZO/Li symmetric cells were galvanostatically cycled at 0.1 mA/cm^2 and 0.1 mAh/cm^2 (Fig. 4c). Li/Pristine-LLZO/Li exhibited a higher overpotential from the beginning and cycled less than 200 h. The poor stability was attributed to the poor interfacial contact and the continuous growth of Li dendrite. Li/LiI-LLZO/Li presented a long cycle life of 2000 h with a stable voltage plateau and a low overpotential (45.3 mV). To further study the interfacial stability with I_2 modification, the Li/LiI-LLZO/Li symmetric cell was also operated at a higher current density of 1 mA/cm^2 with a capacity of 1 mAh/cm^2 (Fig. S6 in Supporting information). During the cycling, the polarization voltage slightly increased from 485 mV to 565 mV. To further evaluate the advantage of LiI interphase, Li/LiI-LLZO/Li symmetric cell was performed at range from 0.2 mA/cm^2 to 0.6 mA/cm^2 for 200 h at per current density (Fig. 4d). The stable polarization voltage was still achieved during the cycling. The polarization voltage corresponded to the previous one when the current density was set back to the same value as the initial one. The corresponding voltage plateaus of different process under galvanostatic cycling was also shown in Fig. 4d. The polarization voltage of Li/LiI-LLZO/Li symmetric cell was stable at 88.3 mV at 0.2 mA/cm^2 in first 4 h and increased slightly to 106.7 mV in last 4 h. The increasing of the polarization voltage was mainly ascribed to the contact loss as the volume changes of Li anode during continuous Li platting and stripping. Even though the contact loss of the solid interfaces is almost unavoidable during electrochemical cycles, the augment of around 20% polarization voltage had limit effect on the electrochemical performance of the symmetric cells. Consequently, attributed to the successful construction of intimate interfacial contact and a thermodynamical stable LiI interphase, Li/LiI-LLZO/Li symmetric cell achieved superior cycling stability, higher CCD in the time/capacity-constant modes and low polarization voltage at various current densities. Fig. 4e compared the time constant mode CCD value and critical capacity. Even though CCD of 1.2 mA/cm^2 was not the highest, considering of the long period for each cycle, the critical capacity of 1.2 mAh/cm^2 showed great advantage among the related literatures.

To evaluate the potential of LiI interphase in practical applications, LMO/LiI-LLZO/Li and LMO/Pristine-LLZO/Li *quasi*-solid-state (with 1.2 wt% liquid content) batteries were assembled for further study. As illustrated in Fig. 5a, the cathode material $LiMn_2O_4$ was mixed with super P and ionic liquid. Toothpaste-like cathode was pasted uniformly on the front side of LLZO, and Li metal was integrated on the bottom of LLZO. All full cells were cycled with a cut off voltage from 3.0 V to 4.3 V at 25 °C. A higher coulombic efficiency and specific capacity were achieved in LMO/LiI-LLZO/Li than LMO/Pristine-LLZO/Li in the first charge and dis-charge cycle

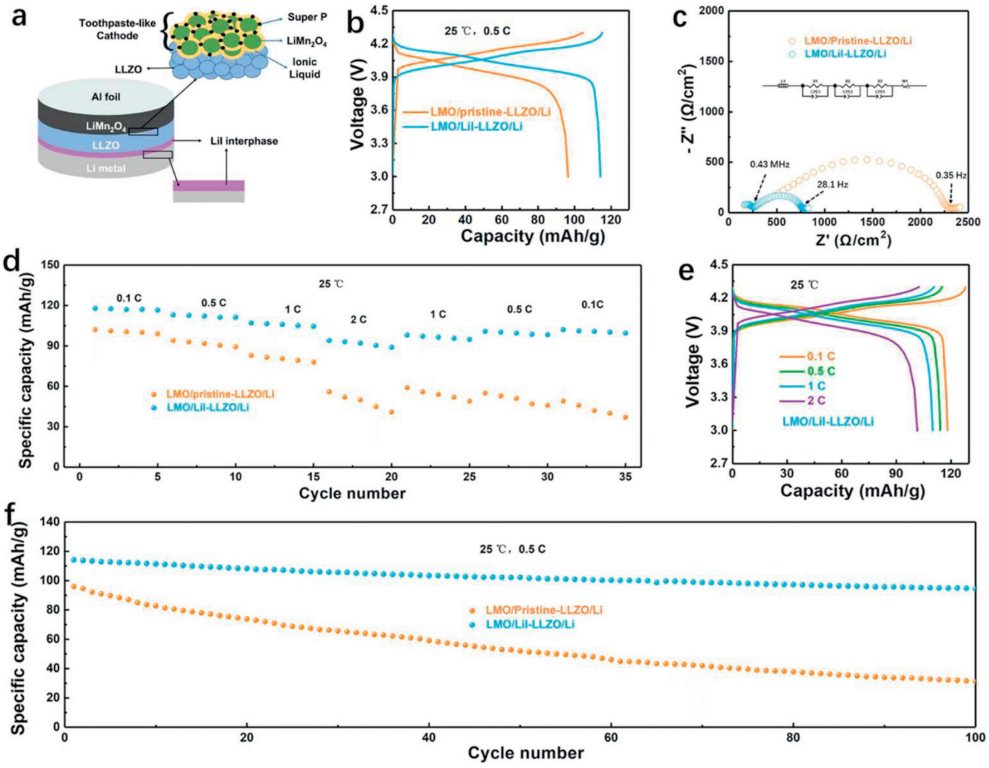

Fig. 5. Electrochemical performance of the quasi-solid-state (with 1.2 wt% liquid content) batteries with and without I_2 modifications. (a) Schematic of the designed battery using LLZO, Li metal anode, $LiMn_2O_4$ (LMO)/super P/ionic liquid composite cathode. (b) Initial charge and discharge curve of LMO/LiI-LLZO/Li and LMO/Pristine-LLZO/Li at 0.5 C. (c) Nyquist plot of LMO/LiI-LLZO/Li and LMO/Pristine-LLZO/Li. (d) Rate performance of LMO/Pristine-LLZO/Li and LMO/LiI-LLZO/Li. (e) Galvanostatic charge and discharge curve of LMO/LiI-LLZO/Li at various rates. (f) Cycling performance of LMO/Pristine-LLZO/Li and LMO/LiI-LLZO/Li at 0.5 C and 25 °C.

at 0.5 C (Fig. 5b). EIS measurement was conducted to characterize the impedance of LMO/LiI-LLZO/Li and LMO/Pristine-LLZO/Li. Both batteries showed approximately equal bulk and boundary resistance above the frequency of 0.43 MHz (Fig. 5c). The overall ASR of LMO/Pristine-LLZO/Li was 2267 Ω/cm^2 while LMO/LiI-LLZO/Li displayed a lower overall ASR of 763 Ω/cm^2. The lower ASR was in accordance with the Li symmetric cells, which was attributed to the improved interfacial contact at the anode side.

Rate performance of both batteries was shown in Fig. 5d. LMO/Pristine-LLZO/Li presented a faster capacity drop than LMO/LiI-LLZO/Li with the current density in-creasing. The corresponding charge and discharge curve of LMO/LiI-LLZO/Li was shown in Fig. 5e. The specific capacity of LMO/LiI-LLZO/Li cell decreased slightly and the voltage platform was around 4.1 V. Fig. 5f showed that LMO/LiI-LLZO/Li also obtained an outstanding cycling performance with a capacity retention of 87% after 100 cycles at 0.5 C and 25 °C while LMO/Pristine-LLZO/Li displayed an inferior cycle stability with only 33% capacity maintained after 100 cycles. LMO/Pristine-LLZO/Li and LMO/LiI-LLZO/Li cells were also tested at a higher current density at 25 °C (Fig. S7 in Supporting information). An outstanding capacity retention of LMO/LiI-LLZO/Li (95%) was achieved compared to LMO/Pristine-LLZO/Li (31%) at 1 C after 50 cycles. The excellent rate and cycle performance of LMO/LiI-LLZO/Li was contributed to the greatly improved LLZO/Li interface, which was not only intimately contact, but also thermodynamical stable. To extend the application of the quasi-solid-state battery with higher energy density cathode materials, the toothpaste-like lithium nickel-cobalt-manganate (NCM811) was also integrated. Fig. S8a (Supporting information) show that the quasi-solid-state battery with LiI interlayer displayed higher initial specific capacity of 171.1 mAh/g at the rate of 0.5 C. The cycling performance in Fig. S8b (Supporting information) also indicated a much higher capacity retention of 80.3% for the NCM/LiI-LLZO/Li *quasi*-solid-state battery after 100 cycles.

We demonstrated an effective strategy to reduce the interfacial impedance and promoting the interfacial stability of the LLZO/Li interface through I_2 modification. The formation of LiI not only reduced the ASR of LLZO/Li from 1525 Ω/cm^2 to 57 Ω/cm^2, but also improved the thermodynamic stability as the effect of electron blocking. The symmetric cells with LiI interphase displayed an ultra-long cycling stability over 2000 h, high CCD value of 1.2 mA/cm^2 in time-constant mode and 7.0 mA/cm^2 in capacity-constant mode, respectively. In addition, the quasi-solid-state battery (with 1.2 wt% liquid content) with I_2 modification presented superior rate performance and impressive cycling stability, which achieved 87% capacity retention after 100 cycles at 0.5 C as well as 95% capacity maintained at 1 C after 50 cycles at 25 °C. Electron blocking and intimate contacted LLZO/Li interface that constructed through the reaction of I_2 with Li achieved outstanding thermodynamic stability and electrochemical performance, which provided an effective strategy for dendrite-free solid-state battery.

Declaration of competing interest

The authors declare that they have no known competing financial interests or personal relationships that could have appeared to influence the work reported in this paper.

Acknowledgments

This work is supported by National Natural Science Youth Foundation of China (No. 22209104), National Natural Science Foundation of China (No. 22179077).

Supplementary materials

Supplementary material associated with this article can be found, in the online version, at doi:10.1016/j.cclet.2023.108846.

References

[1] P. Albertus, S. Babinec, S. Litzelman, et al., Nat. Energy 3 (2018) 16–21.
[2] M. Winter, B. Barnett, K. Xu, Chem. Rev. 118 (2018) 11433–11456.
[3] X. Zhang, A. Wang, X. Liu, et al., Acc. Chem. Res. 52 (2019) 3223–3232.
[4] Y.L. Yang, H.P. Wang, C.L. Zhu, et al., Angew. Chem. Int. Ed. 62 (2023) e202300057.
[5] X.H. Hu, Y. Li, J.D. Liu, et al., Sci. Bull. 68 (2023) 1295–1305.
[6] D. Lin, Y. Liu, A. Pei, et al., Nano Res. 10 (2017) 4003–4026.
[7] J. Liu, H. Yuan, H. Liu, et al., Adv. Energy Mater. 12 (2022) 2100748.
[8] C. Duan, Z. Cheng, W. Li, et al., Energy Environ. Sci. 15 (2022) 3236–3245.
[9] L. Zhai, K. Yang, F.Y. Jiang, et al., J. Energy Chem. 79 (2023) 357–364.
[10] S.B. Yang, B. Wang, Q. Lv, et al., Chin. Chem. Lett. 34 (2023) 107783.
[11] J.C. Bachman, S. Muy, A. Grimaud, et al., Chem. Rev. 116 (2016) 140–162.
[12] R. Chen, Q. Li, X. Yu, et al., Chem. Rev. 120 (2020) 6820–6877.
[13] Z. Zhang, Y. Shao, B. Lotsch, et al., Energy Environ. Sci. 11 (2018) 1945–1976.
[14] Y. Zhu, J.C. Gonzalez-Rosillo, M. Balaish, et al., Nat. Rev. Mater. 6 (2020) 313–331.
[15] Q. Yu, K. Jiang, C. Yu, et al., Chin. Chem. Lett. 32 (2021) 2659–2678.
[16] J.H. Wu, S.F. Liu, F.D. Han, et al., Adv. Mater. 33 (2021) 2000751.
[17] J.H. Wu, L. Shen, Z.H. Zhang, et al., Electrochem. Energy Rev. 4 (2021) 101–135.
[18] N. Zhao, W. Khokhar, Z. Bi, et al., Joule 3 (2019) 1190–1199.
[19] C. Wang, K. Fu, S.P. Kammampata, et al., Chem. Rev. 120 (2020) 4257.
[20] Z. Li, J. Zhang, H.B. Wu, et al., Adv. Energy Mater. 7 (2017) 1700281.
[21] W. Xia, B. Xu, H. Duan, et al., J. Am. Ceram. Soc. 100 (2017) 2832–2839.
[22] X. Han, Y. Gong, K. Fu, et al., Nat. Mater. 16 (2017) 572–579.
[23] A. Sharafi, E. Kazyak, A.L. Davis, et al., Chem. Mater. 29 (2017) 7961–7968.
[24] J.F. Wu, B.W. Pu, D. Wang, et al., ACS Appl. Mater. Interfaces 11 (2019) 898–905.
[25] H. Huo, Y. Chen, N. Zhao, et al., Nano Energy 61 (2019) 119–125.
[26] H. Duan, W.P. Chen, M. Fan, et al., Angew. Chem. Int. Ed. 59 (2020) 12069–12075.
[27] Y. Li, X. Chen, A. Dolocan, et al., J. Am. Chem. Soc. 140 (2018) 6448–6455.
[28] Y. Zhu, J.G. Connell, S. Tepavcevic, et al., Adv. Energy Mater. 9 (2019) 1803440.
[29] H. Xu, Y. Li, A. Zhou, et al., Nano Lett. 18 (2018) 7414–7418.
[30] E.M. Hitz, H. Xie, Y. Lin, et al., Small Struct. 2 (2021) 2100014.
[31] T. Krauskopf, F.H. Richter, W.G. Zeier, et al., Chem. Rev. 120 (2020) 7745–7794.
[32] Y. Shao, H. Wang, Z. Gong, et al., ACS Energy Lett. 3 (2018) 1212–1218.
[33] K.(Kelvin) Fu, Y. Gong, B. Liu, et al., Sci. Adv. 3 (2017) e1601659.
[34] M. Wu, M.Q. Li, Y.M. Jin, et al., J. Energy Chem. 79 (2023) 272–278.
[35] T.K. Schwietert, V.A. Arszelewska, C. Wang, et al., Nat. Mater. 19 (2020) 428–435.
[36] S. Wenzel, T. Leichtweiss, D. Krüger, et al., Solid State Ion. 278 (2015) 98–105.
[37] H. Kwak, S. Wang, J. Park, et al., ACS Energy Lett. 7 (2022) 1776–1805.
[38] F. Han, Y. Zhu, X. He, et al., Adv. Energy Mater. 6 (2016) 1501590.
[39] J.A. Lewis, F.J.Q. Cortes, Y. Liu, et al., Nat. Mater. 20 (2021) 503–510.
[40] S. Wenzel, S. Randau, T. Leichtweiß, et al., Chem. Mater. 28 (2016) 2400–2407.
[41] T. Wang, J. Duan, B. Zhang, et al., Energy Environ. Sci. 15 (2022) 1325–1333.
[42] H. Wan, Z. Wang, S. Liu, et al., Nat. Energy 8 (2023) 473–481.
[43] M. He, Z. Cui, C. Chen, et al., J. Mater. Chem. A 6 (2018) 11463–11470.
[44] J. Duan, W. Wu, A.M. Nolan, et al., Adv. Mater. 31 (2019) 1807243.
[45] Y. Zhu, X. He, Y. Mo, ACS Appl. Mater. Interfaces 7 (2015) 23685–23693.